applied optics

First stellar photons for an integrated optics discrete beam combiner at the William Herschel Telescope

Abani Shankar Nayak,[1,*] Lucas Labadie,[2] Tarun Kumar Sharma,[2]
Simone Piacentini,[3,4] Giacomo Corrielli,[4,3] Roberto Osellame,[4,3]
Éric Gendron,[5] Jean-Tristan M. Buey,[5] Fanny Chemla,[6] Mathieu Cohen,[6]
Nazim A. Bharmal,[7] Lisa F. Bardou,[7] Lazar Staykov,[7] James Osborn,[7]
Timothy J. Morris,[7] Ettore Pedretti,[8] Aline N. Dinkelaker,[1]
Kalaga V. Madhav,[1] and Martin M. Roth[1]

[1]*Leibniz-Institut für Astrophysik Potsdam, An der Sternwarte 16, 14482 Potsdam, Germany*
[2]*Physikalisches Institut Uni Köln, Zülpicher Str. 77, 50937 Köln, Germany*
[3]*Dipartimento di Fisica, Politecnico di Milano, Piazza L. da Vinci 32, 20133 Milano, Italy*
[4]*Istituto di Fotonica e Nanotecnologie—CNR, Piazza L. da Vinci 32, 20133 Milano, Italy*
[5]*LESIA, Observatoire de Paris, Université PSL, CNRS, Sorbonne Université, Université de Paris, 5 place Jules Janssen, 92190 Meudon, France*
[6]*GEPI, Observatoire de Paris, Université PSL, CNRS, 5 Place Jules Janssen, 92190 Meudon, France*
[7]*Durham University, Durham, UK*
[8]*STFC Rutherford Appleton Lab., Harwell Campus, Didcot, UK*
*Corresponding author: anayak@aip.de

We present the first on-sky results of a four-telescope integrated optics discrete beam combiner (DBC) tested at the 4.2 m William Herschel Telescope. The device consists of a four-input pupil remapper followed by a DBC and a 23-output reformatter. The whole device was written monolithically in a single alumino-borosilicate substrate using ultrafast laser inscription. The device was operated at astronomical H-band (1.6 μm), and a deformable mirror along with a microlens array was used to inject stellar photons into the device. We report the measured visibility amplitudes and closure phases obtained on Vega and Altair that are retrieved using the calibrated transfer matrix of the device. While the coherence function can be reconstructed, the on-sky results show significant dispersion from the expected values. Based on the analysis of comparable simulations, we find that such dispersion is largely caused by the limited signal-to-noise ratio of our observations. This constitutes a first step toward an improved validation of the DBC as a possible beam combination scheme for long-baseline interferometry.

1. INTRODUCTION

Aperture masking techniques have been originally developed for infrared (IR) astronomy on large 8–10 m telescopes in order to recover imaging information down to the diffraction limit by forming a non-redundant interferometric array at the pupil of the primary mirror [1,2]. Despite the relatively low throughput of this technique due to the masking of a large fraction of the entrance pupil, aperture masking proved to deliver superior angular resolution in comparison to other competing techniques such as adaptive optics (AO) or speckle interferometry [3,4]. Its high angular resolution makes this technique suitable for the search of close, low-mass companions to nearby stars [5–7]. Pupil remapping extends the concept of aperture masking to the full telescope pupil by breaking it into contiguous sub-apertures coupled to a fiber network that reformats the two-dimensional input pupil into a linearly arranged output pupil [8,9], hence collecting a larger amount of flux. By implementing a waveguide network for pupil remapping on a single, compact, photonic chip, the stability and compactness of the optics system can be increased. In this context, the ability of the ultrafast laser inscription (ULI) technique to write three-dimensional photonic structures in glass ideally enables reformatting from a two-dimensional entrance pupil into a one-dimensional, linear output pupil [10]. The sub-apertures of the output pupil can then be combined interferometrically through

different schemes [11], as for instance a pairwise beam combiner like in GRAVITY and PIONIER instruments [12,13], or a multi-axial, all-in-one, non-redundant scheme as implemented in AMBER and MIRC-X instruments [14,15].

We report here the results of the first on-sky test of a new type of integrated optics interferometric combiner based on the discrete beam combiner (DBC) scheme. The DBC implements the interferometric combination of four telescope beams via an array of 23 evanescently coupled single-mode waveguides arranged in a three-dimensional lattice that ensures coupling beyond the nearest neighbor. For a four-input beam combiner, the complex coherence function of the astronomical source is retrieved from the measurement of the 23 output signals and the inversion of the so-called visibility-to-pixel matrix (V2PM [16]). The DBC operates as a static beam combiner, meaning that instantaneous complex visibilities can be retrieved without any further temporal phase delay using a scanning element. The in-depth description of the DBC's principle and geometry can be found in [17] and references therein.

It is worth noting some specificity of the DBC scheme in comparison to other popular schemes such as the all-in-one multi-axial or the coaxial ABCD pairwise [18] combination schemes. First, since the fringe power is encoded on a minimum number of pixels with each contributing their readout noise, it is advisable to minimize the number of active pixels for the sake of signal-to-noise ratio (SNR) optimization. For a multi-axial combination scheme, the minimum number of encoding pixels per wavelength channel is ∼28 in the four-telescope (4T) configuration and ∼70 in the 6T configuration, respectively [11,19]. The coaxial pairwise ABCD combiner requires 24 pixels in the 4T and 60 pixels in the 6T configuration, while the DBC requires 23 pixels in the 4T and 41 pixels in the 6T configuration [20], respectively. This makes the last two schemes intrinsically more sensitive than the multi-axial scheme [11]. Second, the DBC consists only of straight waveguides in the interaction region, whereas the ABCD pairwise design requires bent waveguides. As bends will induce additional losses in case of a moderate mode confinement, thus affecting the total throughput of ULI written waveguides, the straight waveguides in the DBC design are of advantage. However, there will be bending and transition losses in the bent waveguides or fibers at the pupil remapping stage. The DBC concept has been already validated experimentally (e.g., [20–23]). After initial laboratory tests, on-sky operation is the next important step in order to gain experience in the exploitation of the corresponding observed quantities and qualify it in a realistic observational setting. This was implemented in an observing run with an aperture masking/pupil remapping experiment at the William Herschel Telescope (WHT).

The paper is organized in the following sections: Section 2 briefly recaps the working principle of a DBC. Section 3 describes the design of the device containing the input pupil remappers, DBC, and reformatters at the output. Section 4 describes the fabrication of the device using ULI. Section 5 describes the preparation strategy for performing the on-sky tests at the WHT. Section 6 describes the characterization of the device in obtaining the calibrated V2PM at the telescope. Section 7 shows the on-sky tests obtained from Vega and Altair. Section 8 presents the simulation results of the DBC to explain the deviations for the on-sky results. Finally, the paper is discussed in Section 9.

2. PRINCIPLE OF THE DBC

A description of the theoretical background and working principle of DBCs can be found in the previous work [17,22]. For clarity, we briefly review the definitions relevant for the understanding of the data presented in this paper:

$$\vec{P} = V2PM \cdot \vec{J}, \tag{1}$$

$$\vec{J} = (\Gamma_{11}, \dots, \Gamma_{NN}, \Re\Gamma_{12}, \dots, \Re\Gamma_{N-1N}, \Im\Gamma_{12}, \dots, \Im\Gamma_{N-1N})^T, \tag{2}$$

where $\vec{P}$ represents the power carried across all output waveguides (WGs) and $\vec{J}$ represents the coherence vectors from the observed source. The term Γ_{ii} is the self-coherence (i.e., power at the ith input waveguide or photometry), Γ_{ij} is the mutual-coherence (i.e., complex visibility) of the input light fields, and N is the number of input waveguides. If the transfer matrix (or V2PM [16,22]) is invertible, the coherence vector ($\vec{J}$) can be retrieved from the measurement of $\vec{P}$. The robustness of the retrieval process of $\vec{J}$ by the inverted V2PM can be gauged by the condition number (CN [24]), which describes the propagation and amplification of errors from $\vec{P}$ to $\vec{J}$. Ideally a low, close to unity, CN of the V2PM is desirable. It is, therefore, important to characterize the V2PM of the system since a low CN of the V2PM ensures that the retrieved quantities (i.e., $\vec{J}$) obtained after the inversion are less sensitive to external perturbations of the optical system. A low-conditioned V2PM is achieved by the presence of next-nearest coupling [25], which will be the goal for the fabrication of DBC devices using ULI in Section 4.

The V2PM possesses a pseudo-inverse pixel-to-visibility matrix (in short, P2VM), from which the coherence vectors given in Eq. (2) are extracted. Hence, the Michelson fringe visibility (i.e., normalized amplitude V_{ij}) and its phase ϕ_{ij} can be calculated using [21,22]

$$\left. \begin{array}{l} V_{ij} = \sqrt{\frac{(\Re\Gamma_{ij})^2 + (\Im\Gamma_{ij})^2}{\Gamma_{ii}\Gamma_{jj}}} \\[2mm] \phi_{ij} = \tan^{-1}\left(\frac{\Im\Gamma_{ij}}{\Re\Gamma_{ij}}\right) \end{array} \right\} \quad i \neq j. \tag{3}$$

In stellar interferometry, the actual phase difference from the source cannot be measured due to atmospheric distortion. Even with AO to correct for the atmosphere, there are difficulties in calibrating the point spread function of the AO system [26]. The unknown phase errors coming from a common origin can be canceled by taking a triplet of phases in a closed loop. The resulting term is called the closure phase (CP), a quantity that can be used directly for high contrast images in stellar interferometry [27,28]. The CP is defined as

$$\Phi_{ijk} = \phi_{ij} + \phi_{jk} - \phi_{ik}, \tag{4}$$

where Φ_{ijk} is directly calculated from the pairwise retrieved phases (ϕ_{ij}) given by Eq. (3). Note that a stable solution for the CP can only be obtained when $\vec{J}$ is extracted from a P2VM with all the N input beams injected simultaneously. We, therefore, show results of the CP in Sections 7 and 8, as these

measurements involved simultaneous injection of light to all four DBC inputs. We will use the notations given by Eqs. (3) and (4) throughout the paper to describe the results obtained from the DBC.

3. DESIGN OF THE DBC

The structure of the device employed for the on-sky test at the WHT can be divided into three main parts and is shown in Fig. 1. The core of the circuit is represented by the zig-zag DBC, composed of 23 waveguides interacting through evanescent coupling and arranged in two different planes [Fig. 1(b)]. This geometry allows the presence of both a nearest coupling between adjacent waveguides on the same plane, and a next-nearest coupling between the neighboring waveguides belonging to different planes. The coupling can be independently controlled by selecting the vertical separation between the planes and the planar distance between the waveguides. Before the DBC, a pupil remapper composed of four single-mode waveguides is inscribed, with the role of injecting light into the four inputs of the DBC. The principle of the pupil remapper is to collect light from separate sub-apertures of the telescope and combine them coherently to measure the complex visibilities as given by Eq. (3). The position of four inputs of the pupil remapper is shown in Fig. 1(a). This arrangement was chosen such that the input facet of the device is placed in a reimaged telescope pupil, which has been hexagonally segmented using a 37 segmented deformable mirror, allowing the control of coupled light into each of the four input waveguides of the pupil remappers. An augmented positioning of the 37 segments (i.e., upper half) of the deformable mirror projected on the input facet of the chip containing the pupil remappers is shown in Fig. 2(b). Note that, in the rest of the paper, we use the expression *deformable mirror* (and its acronym DM) to indicate the segmented deformable
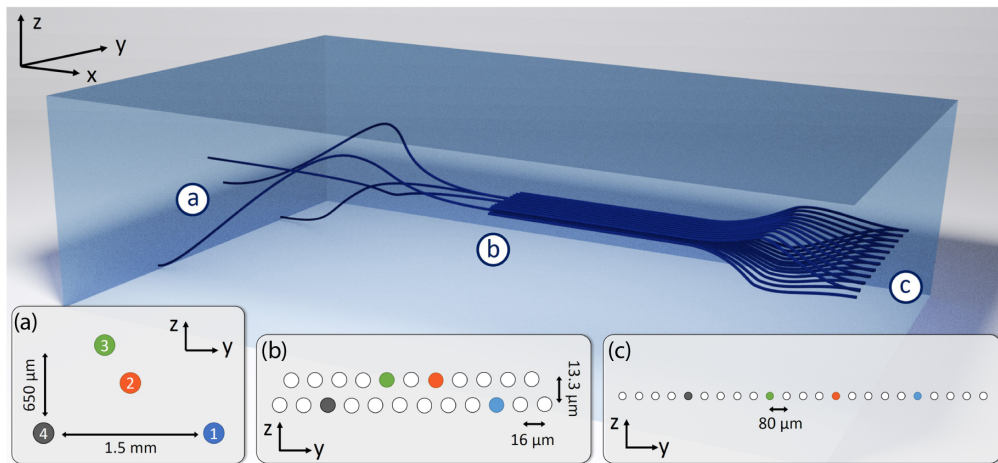

Fig. 1. Design of the beam combiner with pupil remapper and fan-out. (a) Section showing the arrangement of the four input waveguides of the pupil remapper. The input face of the pupil remapper is placed in a reimaged telescope pupil, which has been hexagonally segmented using a segmented deformable mirror [see Fig. 2(b)]. (b) Section of the zig-zag DBC. The four input waveguides are highlighted in color, together with the horizontal and vertical pitches of the array. (c) Output section of the device, after the reformatting performed by the fan-out region. The waveguides are linearly arranged, with a separation of 80 μm.
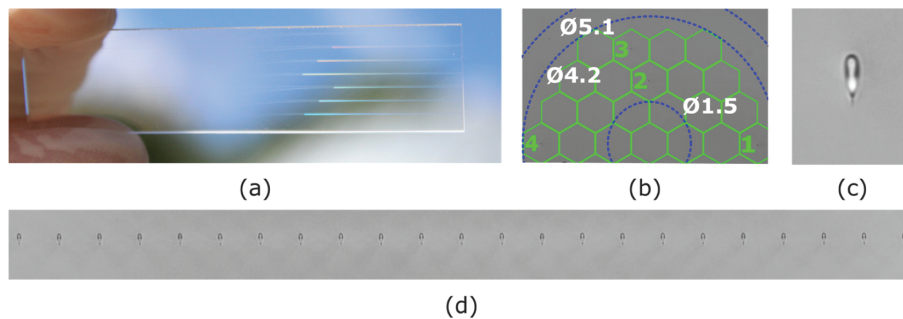

Fig. 2. Images showing parts relevant to the integrated optics chip and its interface with the segmented mirror *(not to scale)*. (a) Integrated optics chip inscribed in an alumino-borosilicate glass from Politecnico di Milano. The chip contains several devices with the geometry shown in Fig. 1 but differing in two design parameters: the vertical distance between the horizontal planes, ranging from 11.8 μm to 13.8 μm, and the DBC length, from 18 mm to 22 mm. The device that was used for on-sky operation is shown in the micrographs (b)–(d). The waveguides are faintly visible in scattered light. (b) Input facet of the chip. Dimensions shown in white are in mm. The four input waveguides can be barely seen. The image is overlaid with a green grid showing the projection of a hexagonal-shaped segmented deformable mirror (DM) used to steer light in the waveguides. The numbering of the input pupil remappers is also marked and followed throughout the paper. The innermost and outermost blue overlay shows the projection of 1.2 m obscuration and 4.2 m primary of the WHT, respectively. The middle blue overlay shows the 4.2 mm diameter of the DM. (c) A magnified view of the single-mode waveguide written in the device using ULI. (d) Output facet showing the linear arrangement of 23 waveguides of the device.

mirror used in the DBC experiment. This is not to be confused with the deformable mirror used by the CANARY AO system itself.

For designing the waveguides of the pupil remapper, we employed a MATLAB custom routine implementing a recursive cubic spline interpolation. This software allowed the equalization of the geometrical paths of the injected light beams [29] with an error lower than 1 nm, thus preserving their coherence before reaching the DBC. The minimum radius of curvature was set at 30 mm for not introducing additional losses. After the beam combiner, a fan-out region was added to remap (in other words, reformat) the output section from a zig-zag configuration to a linear one [Fig. 1(c)]. This approach makes the output modes more distinguishable since they can be arranged with higher separations. Moreover, it would make a spectral measurement easier, since the output light could be vertically dispersed without the risk of modal cross talk. Like the pupil remapper, the fan-out waveguides were designed with spline functions, implementing an isotropic expansion of the array for keeping uniform the coupling between the nearest neighboring waveguides. Since in the first part of the expansion the waveguides are still slightly coupled, we properly reduced the length of the DBC for obtaining the same effective length. The design of the integrated optics input remapper is constrained by the geometry of the entrance pupil array [see Fig. 2(b)] to be remapped. The marked segments 1, 2, 3, and 4 were chosen to build a non-redundant array containing both long and short baselines.

4. FABRICATION

For the fabrication of the device, we employed a cavity-dumped Yb:KYW source, delivering pulses with a central wavelength of 1030 nm, duration of 300 fs, and repetition rate of 1 MHz. The optimal inscription process for obtaining low-loss single-mode waveguides at 1550 nm consisted of focusing the laser beam with a power of 620 mW through a $50\times$, 0.6 NA microscope objective inside an alumino-borosilicate glass (Eagle XG by Corning), translated by an air-bearing motion stage (Aerotech FiberGlide 3D) at a speed of 40 mm/s. The translation was performed 6 times for each waveguide for increasing the induced refractive index contrast. After inscription, the device was subjected to a thermal annealing, consisting of a 1 h long heating step up to 750°C, followed by a slow cooling, first with a rate of -12°C/h down to 630°C, then with a rate of -24°C/h down to 500°C, followed at the end by a natural cooling down to room temperature. This treatment reduces both the waveguides birefringence and the losses since it releases the internal stresses generated during the laser inscription [30,31]. The result of the complete fabrication process is a single-mode waveguide suitable for operation at 1550 nm with propagation losses of about 0.2 dB/cm, a $1/e^2$ mode dimension of 8.5(3) μm × 9.0(3) μm, and a birefringence value below 5×10^{-6}. It is worth noting that the fabricated waveguides showed very similar performances regardless of the inscription depth, allowing, therefore, the fabrication of a pupil remapper with almost identical waveguides. However, when increasing the inscription depth for waveguides more buried in the glass, we observed a reduction of the vertical offset between the center of the guiding structure and the point where the inscription

laser was focused. This effect is probably related to the dissimilar focusing conditions occurring at different depths due to spherical aberrations. Since this change of the offset could lead to a misalignment between the focal spot of the telescope segments and the device inputs, we applied a depth-dependent correction factor to the vertical coordinates of the four input waveguides during the writing process.

After the optimization of the inscription parameters, we fabricated preliminary zig-zag DBCs and studied the dependence on the waveguide distance of the planar and diagonal coupling coefficients, defined as the angular frequency of the optical power beating in a system composed of two evanescently coupled waveguides. With an in-plane pitch of 16 μm and a separation between the planes of 13.3 μm, we were able to obtain the same value for both coupling coefficients, equal to 1 cm^{-1} at 1550 nm (in a system of two coupled waveguides, such a value would guarantee a full optical power transfer after a length of about 1.5 cm). With this value, the interaction length of the combiner was set to 20 mm to provide the lowest CN of the V2PM according to the simulations. We employed these geometric parameters for the fabrication of the DBC with pupil remapper and fan-out used in the on-sky experiment. The characterization of the device with horizontally and vertically polarized light provided the same output distributions, thus validating its polarization insensitivity. Finally, by coupling the device with an SMF-28 fiber, the insertion losses were measured to be lower than 3 dB for all the four inputs, corresponding to a transmission of ~50% for a total length of the chip of 7.5 cm.

5. PREPARATION FOR THE ON-SKY CAMPAIGN

A. Laboratory Characterization of the Integrated Optics Device

We first conducted a systematic laboratory characterization of the different manufactured beam combiners in order to identify the most suitable DBC to be operated at the telescope. We considered the following tasks: (1) obtaining temporal fringes at all the 23 output waveguides for all baseline combinations; (2) getting a low-conditioned V2PM of the device. To identify the best component, we used a Michelson interferometer setup [20] to record pairwise temporal fringes, determine the V2PM, and extract the visibilities. We used a tunable laser source for the V2PM characterization. Although the device was designed at 1550 nm, we were able to get a low-conditioned V2PM at slightly longer wavelengths, namely around 1600 nm due to breaking of the phase symmetry obtained from a DBC [25]. The V2PM CN was measured to be ~10.5 at 1600 nm. The extracted complex visibilities are shown in Fig. 3 in [32]. We then used a broadband source in combination with different filters to identify the best bandwidth for the on-sky operation. The previous studies have shown that our DBC device should operate with a moderate bandwidth due to residual phase errors of $\leq \frac{\pi}{2}$ from the retrieved complex visibilities [23]. We identified an optimal result in conjunction with a $\Delta\lambda = 50$ nm bandpass filter (see Fig. 2 in [33]) for the retrieved visibilities with a CN of ~11.4.

B. Design of the Experiment

To interface the device with the WHT, we designed an experimental layout using Zemax modeling. In our case, two main components are required for pupil remapping of the WHT. First, the reimaged WHT pupil has to be hexagonally segmented using a DM. Second, the light from the individual segments has to be coupled into the pupil remappers, for which a microlens array (MLA) was used. Recent examples of such a configuration can be found in [10,34]. For this purpose, we used a DM consisting of 37 hexagonal segments from Iris AO, Inc., and a MLA from SUSS-MicroOptics with a back focal length of 910 μm, the schematic of the setup is shown in Fig. 3. The coordinates of the four sub-apertures projected onto the WHT primary are provided in Table 1.

Table 1. Coordinates of the Sub-Pupils Projected onto the Telescope Primary in the Reference Frame of Fig. 2(b)

	Sub-Pupil 1	Sub-Pupil 2	Sub-Pupil 3	Sub-Pupil 4
x (meters)	+1.52	0	−0.24	−1.52
y (meters)	0	+0.85	+1.32	0

From the WHT, the $f/11$ corrected beam enters our setup, where the achromatic lens L1 collimates the light to a beam with diameter of 11.4 mm. The collimated beam after lens L5 had a diameter of 5.1 mm, which is ∼20% larger than the 4.2 mm diameter of the inscribed circle of the DM. The DM has a pitch of 606.2 μm, and that of the MLA is 250 μm. Hence, we used
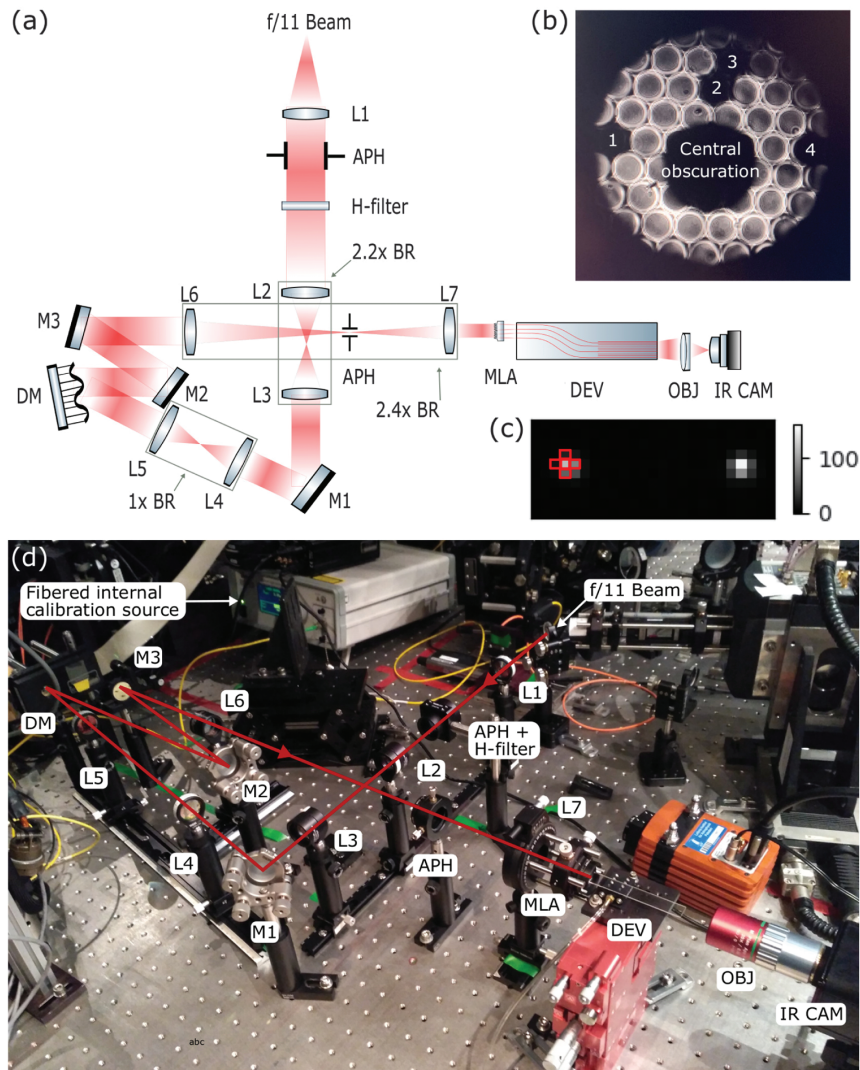

Fig. 3.   (a) Schematic of the optical setup that was used on the WHT Nasmyth bench (*not to scale*). $f/11$ is the AO corrected beam that is received from the WHT. The following acronyms are used: L, lens; H-filter, H-band filter ($\lambda_0 = 1600$ nm, $\Delta\lambda = 50$ nm); APH, adjustable pinhole, BR, beam reducer; M, mirror; DM, segmented deformable mirror; MLA, microlens array; DEV, device under test; OBJ, objective; IR CAM, infrared camera. The various focal lengths are f1 = f4 = f5 = f7 = 125 mm, f2 = 100 mm, f3 = 45 mm, f6 = 300 mm. (b) Image to verify the conjugation of the DM onto the MLA before injection into the integrated optics (IO) device. The sub-apertures to be coupled into the IO device are steered out by tilting the corresponding segments of the DM and appear therefore in black. (c) Two of the output waveguides of the DBC after bias subtraction with Vega's starlight injected into the device. The image is magnified by a factor of ≈3.4, and the colorbar shows the analog-to-digital units (ADU). Also shown is a red augmented area consisting of 5 pixels, which is used to calculate the power across each output waveguide. (d) Photograph of the optical setup as installed on the Nasmyth platform with the red beam illustrating the light path from the telescope to the IO device.

two sets of achromatic lenses L6 and L7 to reduce the beam by a factor of 2.4 to achieve good conjugation between the DM and MLA pitches. By reducing the beam size, we can also avoid unwanted overlap of different segments of the DM on the same MLA lenslet as well as spurious injection of light from a nearby MLA lenslet into the integrated optics device.

The average total throughput of our system is at most ~ 4 % (see Table 2) The numerical calculations based on the overlap integral showed that a coupling efficiency of ≈78% could in principle be achieved when considering the numerical aperture of the individual MLA lenslet and the mode field diameter of the input single-mode waveguides of the device. Each individual MLA lenslet produces a 49.4 cm aperture when projected on-sky, which is less than the Fried parameter calculated at 1600 nm, as shown in Table 3. Hence, the wavefront across the MLA aperture can be assumed to be parallel, and the on-sky coupling efficiency could, if the optimal alignment is reached, be close to the theoretical limit. However, we are in practice limited by the thermo-mechanical stability of the setup, which ultimately probably decreases the effective coupling efficiency. A long distance (≈80 cm) between the DM and MLA was kept to make sure that the individual DM segments could be steered out of the optical path when maximum tip/tilt (+/ − 2 mrad) was applied.

We used two InGaAs cameras: Ninox 640 from Raptor photonics and CRED2 from FIRST Light. All images recorded by the camera were stored in the FITS file format. For characterization and extraction of the V2PM, the Ninox 640 was used since we had the software for synchronous control. For the on-sky measurements, we switched to the CRED2 because of its lower dark current and readout noise. However, we did not have the necessary software for synchronous control of the CRED2 with the DM, which is required to determine the V2PM.

6. CHARACTERIZATION AT THE TELESCOPE

We used the broadband source from Amonics as an internal calibration source to obtain the V2PM at the WHT. The light

from the broadband source was launched into the optical path such that it could include all the necessary components to obtain the transfer function of the system located after the Nasmyth focus of the telescope. This included the CANARY AO system [35,36] as well as the optical elements of our DBC experiment. The AO system was turned off during calibration, which corresponds to a close to flat configuration of the ALPAO deformable mirror. For the initial calibration, our DM was also flattened, corresponding to a configuration of zero phase reference for the four injected beams.

With the calibration source launched into the optical path, we used the DM and MLA to couple the chosen four sub-apertures into the device as shown in Fig. 2(b). The remaining 33 unwanted focal spots formed by the MLA were steered away. We first optimized the coupling in each input waveguide by tip-tilting the corresponding segment. As the default ± 2.5 µm piston range of the DM segments was influenced by the applied tip-tilt, this resulted in each segment having a slightly different total travel range. However, within this travel range, we made sure that the piston sampling was fixed at 5 nm/frame.

We proceeded with the usual V2PM characterization: first, by injecting only one input beam to record the single excitation; second, by injecting two input beams to record the pairwise excitation. The temporal fringes at the output were recorded by delaying the corresponding DM segment. With this process, we recorded four single excitations and six pairwise excitations of the input light beams to generate the 16×23 elements of the V2PM. We show the visibility amplitudes in Fig. 4 extracted from one of the low-conditioned V2PM that was acquired at the WHT with the calibration source. The CN was 12.5, slightly higher than that obtained in the lab using the two-beam Michelson setup (see Section 5).

The mean squared error between the theoretical value and the experimental curve in blue for visibility amplitudes in Fig. 4 is in the range $0.4-7.4 \times 10^{-2}$ for all visibility pairs. This range of mean squared error is of the same order of magnitudes as the visibility amplitude obtained from the two-beam Michelson setup in the lab. However, the mean squared error
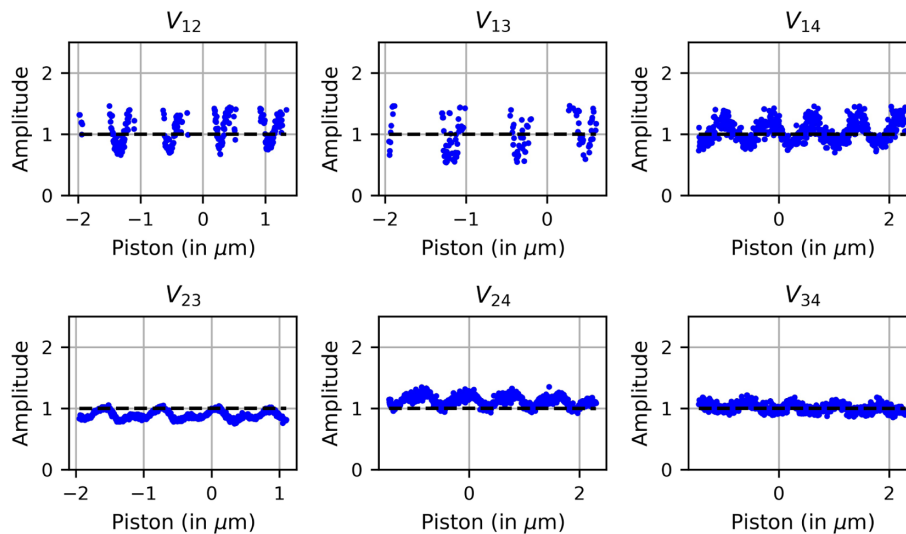

Fig. 4. Retrieved visibility amplitudes from the V2PM data shown in blue, obtained at the telescope using the calibration light source ($\lambda_0 = 1600$ nm, $\Delta\lambda = 50$ nm). The oscillations are due to residual phase errors obtained from a chromatic V2PM [23]. The missing amplitude values for V_{12} and V_{13} are due to the photometry imbalance (see Section 6).
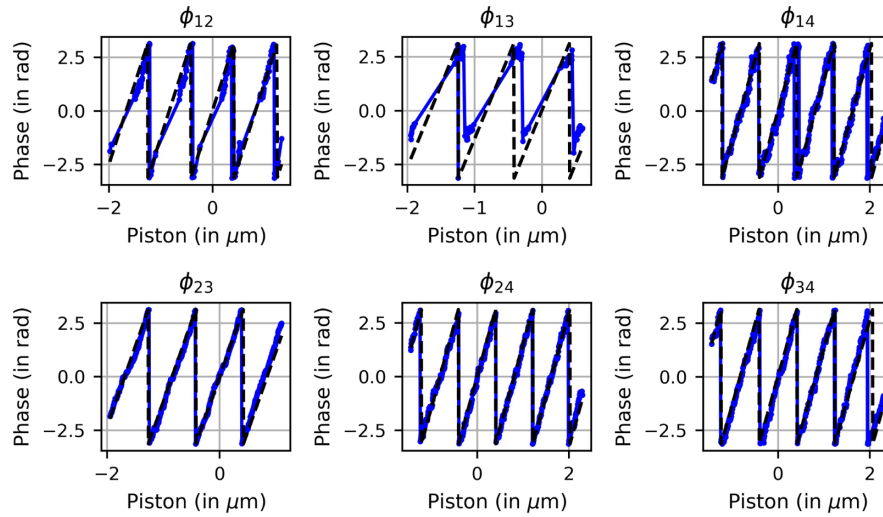
Fig. 5. Retrieved visibility phases from the V2PM data shown in blue, obtained at the telescope with the calibration source. The black line shows the theoretical value.

of the visibility amplitude pairs, especially ($V_{12} = 5.0 \times 10^{-2}$, $V_{13} = 7.4 \times 10^{-2}$, and $V_{14} = 2.8 \times 10^{-2}$), is slightly higher in comparison to the other three pairs, which is evident in Fig. 4. We used a statistical approach where we defined a confidence interval and showed only those frames for the retrieved visibility amplitudes, whose value was within 50% of the theoretical value of visibility amplitude in Fig. 4. We discarded those frames that were outside the 50% confidence interval, which happened due to larger imbalance originating in the retrieved photometry [i.e., Γ_{ii} in Eq. (2)] of the input waveguide numbered 1. The photometry imbalance ($= \Gamma_{ii}/\Gamma_{jj}$) for V_{12} and V_{13} was a magnitude higher than the remaining four visibility pairs. As a result, the V_{ij} value given by Eq. (3) deviates from the expected amplitude value and falls outside of the confidence interval defined above, implying missing values for V_{12} and V_{13} in Fig. 4. This might have happened due to coupling errors at input 1 from the DM segment in between the pairwise excitation of two input beams, while obtaining the V2PM.

The confidence interval defined above for the visibility amplitudes was then used to calculate the retrieved visibility phases as shown in blue in Fig. 5. The theoretical phase is shown in black with a spatial frequency of $\sim 4\pi/\lambda$. There is a factor 2 in the spatial frequency due to the reflection on the DM. Figure 5 shows a close match between the retrieved and the theoretical values, except for ϕ_{12}, ϕ_{13}. The phase deviation for the latter is suspected to be due to residual phases caused by coupling errors as mentioned above, as well as uncertainties in the piston positioning of the DM segment.

The above calibrated P2VM obtained at the WHT is applied to the stellar targets and the visibilities are extracted in the subsequent sections.

7. ON-SKY TESTS

We performed the on-sky tests during the nights of August 9–12, 2019, with observing conditions summarized in Table 3. We observed the two bright stars Vega and Altair (H $\sim$ 0) subtending an angular resolution of a few milliarcsecond (mas)

and, thus, appearing as point sources at the spatial resolution of the WHT. These two sources, which are among the brightest stars in the Northern hemisphere, were selected based on their observability (right ascension and declination) during the entire night. We have operated with the support of the CANARY AO system to compensate for the atmospheric turbulence. We briefly describe the AO system from where we obtained the $f/11$ corrected beam. CANARY is a multi-guide star AO system that was developed to demonstrate multi-object AO correction. CANARY was configured in single conjugate adaptive optics (SCAO) mode with an expected throughput of <15% for this experiment. In this mode, CANARY uses a 14×14 sub-aperture Shack–Hartmann wavefront sensor controlling a 241-actuator deformable mirror from ALPAO at a frame rate of 150 Hz [35–37]. When CANARY is operated in SCAO mode, and depending on the seeing conditions, an average Strehl ratio (SR) of 0.3 is obtained. In Table 3, we report the actual range of wavefront errors delivered by CANARY during the observation of our sources.

We used the four segments of the DM to couple light into four inputs of the pupil remapper via the MLA (see Fig. 3). We used the CRED2 camera water-cooled at 233 K and affected by a readout noise of $\sim 22e^-$ [38] to record the DBC outputs. Since we did not have the routines for a synchronous control

Table 2. Estimated Throughput of Our System Down to the Infrared Camera[a]

Components	Throughput (in %)
CANARY (e)	<15
Optics (e)	66
Coupling efficiency (e)	78
DBC device (m)	$\sim$50
Total	$\sim$3.9

[a]In brackets, "m" refers to measured and "e" to estimated throughput. For the coupling efficiency, we emphasize that we report here the optimistic upper limit. The effective on-sky coupling efficiency could not be measured. The optics include H-band pass filter (T = 90%), lenses (T = 99.5%), mirror (R = 96%), and MLA (T = 90%).

Table 3.   Table Showing Different Averaged Quantities Describing the Observing Conditions for the Nights: Seeing Values Recorded from the Metrology Archive of the WHT at 500 nm, the Fried Parameter Calculated at 1600 nm, Wind Speed, Atmospheric Time Constant, Range of Root-Mean Squared Wavefront Errors from CANARY, and Stellar Targets Observed Per Night

Nights	Seeing (arcsec)	$r_0{}^a$ (cm)	v^b (km/hr)	$\tau_0{}^c$ (ms)	$\sigma_\lambda{}^d$ (nm)	Targets
10–11	0.7	58.3	20	32.5	169.2–276.5	Altair
11–12	0.8	50.8	20	28.3	295.9–432.3	Vega

$^a r_0$ represents Fried parameter.
^{b}v represents wind speed.
$^c \tau_0$ represents time constant.
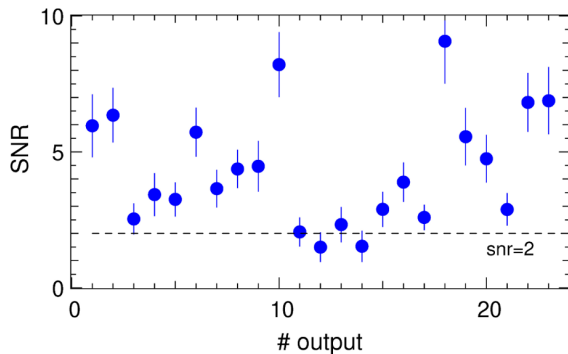$^d \sigma_\lambda$ represents wavefront error.

Fig. 6.   Measured flux SNR at each of the 23 outputs while observing Vega. Note that no frame selection is considered here. The dashed line corresponds to SNR = 2.

of the CRED2 and DM, we had to use the CRED2 and DM interfaces separately. The DM interface was used to steer in the four DM segments without adding any additional piston. The CRED2 interface was used to record various sets of 1500 frames in one continuous shot. All the frames were bias-subtracted. The bias frames were recorded by blocking the starlight path with a physical aperture placed before L1 (see Fig. 3).

The exposure time per frame was chosen to be $t_e = 250$ ms with the CRED2 camera in high gain mode. The choice of this value was motivated by the necessary compromise between the SNR and risk of fringe smearing. As we were not in the position to analyze in real-time the quality of the delivered AO correction and the delivered SNR at the DBC outputs, we relied on values adopted by other similar near-IR experiments [10] for which the interferometric fringes were detected using $t_e = 200$ ms and without any assistance of external AO acting as a fringe tracker. Figure 6 reports the typical SNR measured at each of the 23 outputs of the DBC when observing Vega.

For the subsequent data reduction, we selected a crossed region of five pixels around the peak value [see Fig. 3(c)]. For the analysis of stellar targets, we applied the frame selection according to the following criteria: first, the extracted power of the output waveguides has to be positive. The frames with power of <0.1 counts were discarded. Second, when retrieving the input power [Γ_{ii} in Eq. (2)] by applying the P2VM to the data, the frames resulting in negative values were removed. Third, we considered only those frames with the retrieved visibility amplitudes in the range 0–4 to show our on-sky results.

A. Vega

We report in Fig. 7 and Fig. 8, respectively, the histograms of the retrieved visibility amplitudes and CPs obtained on Vega. With the selection criteria defined above, 84% of the frames out of 10,500 frames contributed to the pool of data. The calculated mean, standard deviation, and median values are reported in Table 4. The histograms exhibit a Gaussian skewed shape peaking to $\sim 0.6-0.9$. While the expected visibility value for a point source is close to 1, our measurements are impacted by partial AO correction and longer integration times, which may result in fringe smearing (see Section 8.D). The visibility spread is significant, about 0.4 on average. This suggests that the retrieval process through the inverse V2PM is unstable, possibly due to the overall low flux level (see Section 8). The mean value of the CP is ~ 0 for Φ_{124}, Φ_{134} as expected for a point source, whereas it is offset for the other two triplets. Similarly, a significant spread is seen in the CP histograms. From the V2PM inversion, we also retrieved the four input photometries corresponding to the Γ_{ii} terms in Eq. (2) (see Fig. 9) and reported them in Table 5 for comparison between Vega, Altair, and the calibration source.

B. Altair

We recorded only one continuous shot for Altair with a total of 1500 frames. As shown in Table 5, the photon number from Altair is comparable to the case of Vega, which suggests that the error analysis and potential impact of noise sources in low photon regime may apply to the Altair data as well. We show the visibility amplitudes and CPs for Altair in Figs. 7 and 8, respectively, where contributions from 94% of the frames are shown for the analysis of the visibilities with the selection criteria defined above. The mean, standard deviation, and median values of the visibilities for all combinations from Altair are shown in Table 4.

C. Discussion of On-sky Results

Figures 7 and 8 present the results on the retrieval of the coherence function in a way that several hypothesis can be advanced to explain the spread of our data. The third row reports the visibilities retrieved from the observation of our internal calibration source, which corresponds to a high-flux level case at the inputs of the DBC (see Table 5). The fourth row shows the results of the visibilities retrieval from a region of the detector fully dominated
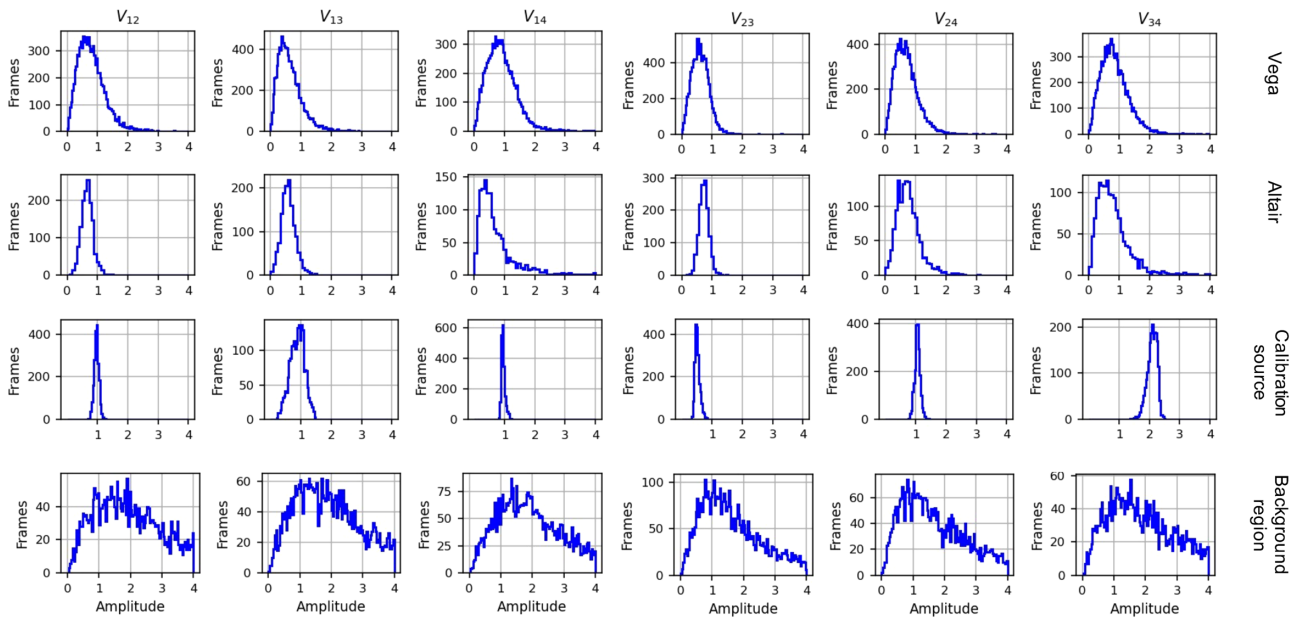
Fig. 7.   Histograms of the visibility amplitudes for Vega, Altair, the calibration source, and a background region.
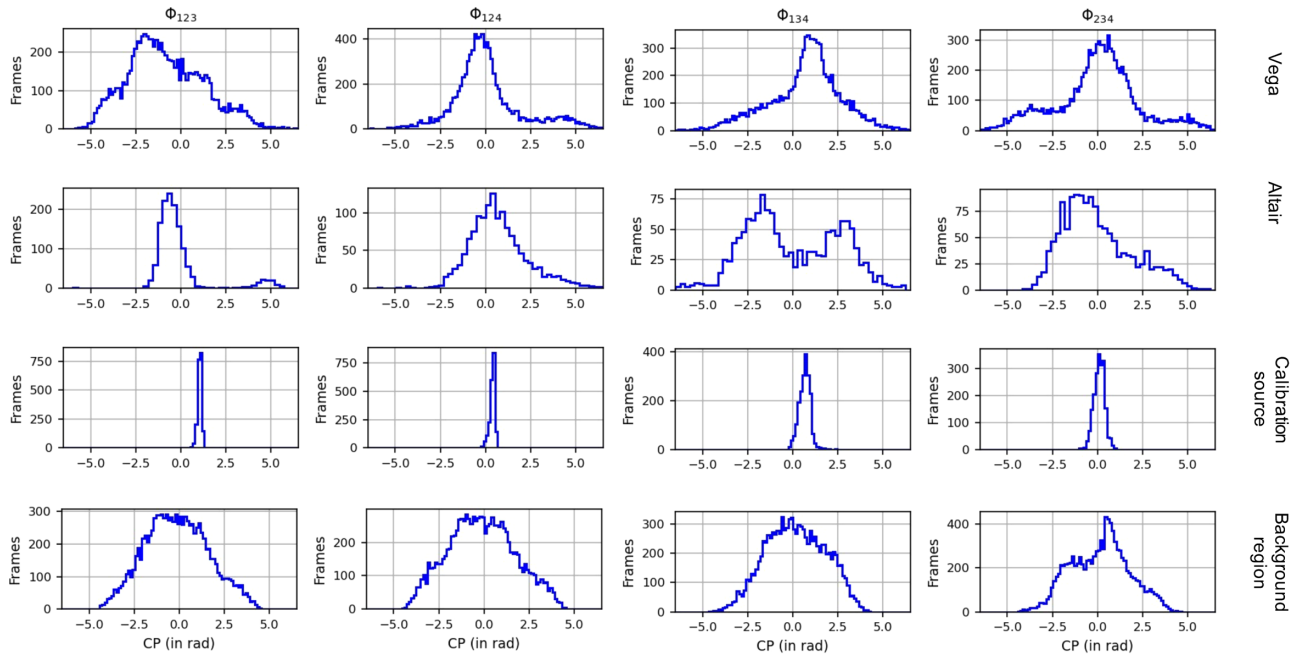

Fig. 8.   Histograms of the closure phases for Vega, Altair, calibration source, and a background region.

by the background and its noise. For all of these four cases, the *identical* V2PM obtained from Section 6 has been employed.

### 1. Impact of Photon Noise and Detector Noise

Considering the low throughput of our experiment together with intrinsically small diameter of the individual sub-apertures, we are probably in a photon-starving regime despite observing two of the brightest stars in the northern hemisphere. We observe in Figs. 7 and 8 that the histogram of the retrieved coherence function for the calibration source is much more peaked, owing to the much larger amount of flux collected as seen in

Table 5. On the contrary, when applying the retrieval process to a detector region totally dominated by the background noise, the corresponding histograms present the widest spread both for the visibilities and CPs. In the case of Vega, although stellar photons are collected at the 23 outputs, the modest SNR measured (see Fig. 6) clearly point at a photon-starving regime. Note that the visibility amplitude histograms obtained for Altair appear slightly less spread than in the case of Vega. It could be that an improvement of the throughput (see Table 5)—caused for instance by the better AO correction on Altair (see Table 3) or a more stable coupling—has helped toward more stable results. However, the effect remains marginal and cannot be

Table 4.   Mean, Standard Deviation, and Median Values for the Visibilities and Closure Phases Obtained for Vega and Altair

Vega		Visibility Amplitudes						Closure Phases (in rad)			
	V_{12}	V_{13}	V_{14}	V_{23}	V_{24}	V_{34}	Φ_{123}	Φ_{124}	Φ_{134}	Φ_{234}
Mean	0.81	0.64	0.91	0.60	0.69	0.85	−0.85	0.08	0.67	−0.02
Std[a]	0.48	0.43	0.52	0.28	0.38	0.47	2.11	1.99	2.05	2.34
Median	0.73	0.55	0.84	0.58	0.64	0.78	−1.10	−0.23	0.89	0.13
Altair										
Mean	0.65	0.58	0.70	0.72	0.75	0.76	−0.13	0.72	−0.13	−0.04
Std[a]	0.19	0.23	0.63	0.16	0.39	0.51	1.59	1.64	2.70	1.92
Median	0.65	0.56	0.51	0.72	0.69	0.67	−0.53	0.49	−0.66	−0.39

[a]Std represents standard deviation.
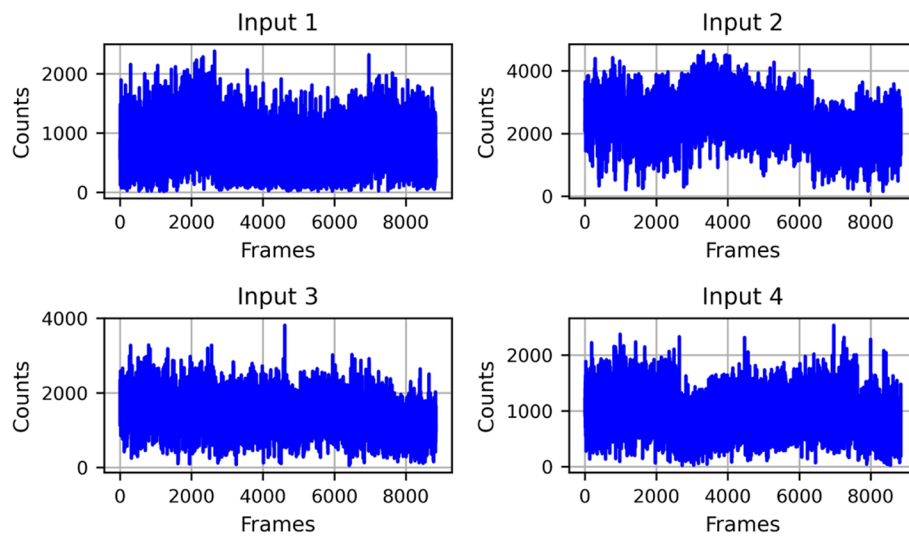
Fig. 9.   Plots of the retrieved photometry for the four inputs of the DBC for Vega.

Table 5.   Retrieved Photometry of the Four Inputs When Injected Simultaneously into the DBC Combiner

Γ_{ii} (in Camera Counts)	Calibration Source	Vega	Altair
Input 1	$56,000 \pm 3000$	800 ± 400	1700 ± 500
Input 2	$128,000 \pm 6000$	2300 ± 700	2500 ± 600
Input 3	$41,000 \pm 4000$	1400 ± 500	1500 ± 300
Input 4	$51,000 \pm 3000$	900 ± 300	700 ± 300

fully proven at this point. A simulation of the impact of the photon shot noise and detector noise is presented in Section 8 to support these findings.

2. Partial AO Correction and Decoherence

We are using AO correction as an external fringe tracker to maintain coherence between the sub-apertures. Because of partial AO correction, the relatively long integration time adopted may still lead to temporal decoherence, hence decreasing the values of the retrieved visibilities. When looking at the visibility amplitude distribution obtained with the calibration source, the histograms show a rather limited spread and have a median value close to $V = 1$, except for V_{23} and V_{34} for a reason that we cannot make explicit at this point. Similarly, the CP histograms are also comparatively narrow, with a median value

for Φ_{124}, Φ_{234} triplets close to 0° when compared to the other two triplets. Clearly, the partial AO correction combined with a longer integration time leads to some decoherencing, which explains partly the retrieved visibility amplitudes smaller than 1 for Vega and Altair. Since the CP is an observable more robust to external phase errors, we may have expected a more peaked distribution for the two stars. But again, the overall low-level of light flux might result in random phase errors, which is detrimental for a robust calibration of the CP signal. This effect is also analyzed through simulations in Section 8.

3. V2PM Calibration

Finally, we suspect that our process to derive the V2PM of our system may also lead to the generation of systematic biases that are difficult to identify. Indeed, due to configuration issues,

we have used the Ninox 640 to establish the V2PM and the CRED2 for the on-sky and internal calibration measurements. Because of the different levels of detector noise between the two cameras, this may lead to the presence of biases. This fact is confirmed for the calibration source, where the retrieved visibilities are not the same for all the pairs and CP triplets. Finally, although the experimental CN is not particularly high compared to other laboratory experiments [21], the value of CN = 12.5 may still suggest a limited stability of the coherence-retrieval procedure.

8. SIMULATION

In order to better understand the on-sky results and their deviations from the expected values for visibility amplitudes and CP, we used BeamPROP from Rsoft to simulate a DBC device with parameters close to those of the device used in the current experiment. We simulated only the DBC interaction region as shown in Fig. 1(b) with the electric fields launched in the four inputs to obtain the V2PM at 1.6 μm and successively retrieve the coherence functions. We underline that a simulation taking fully into account the properties of the CANARY AO, DM, and MLA is beyond the scope of this paper. As a consequence, we simplify the description of the electric fields being launched in the present analysis. From the SR of ∼30% delivered by CANARY, we derived a wavefront error of $\lambda/5.7$ rms and varied the relative phase between the four input electric fields using a random Gaussian distribution with a standard deviation of $2\pi/5.7$. We also accounted for amplitude fluctuations at the four inputs in the form of a random Gaussian distribution with a mean of 1 and a standard deviation of 0.3, as well with strictly positive amplitude values. In the subsequent sections, we show the results of the simulation study.

A. Input Amplitude and Phase Errors

We obtained 500 realizations of the output images of the DBC produced by Rsoft and applied the simulated P2VM described above to extract the visibilities. The retrieved visibility amplitude is shown in Fig. 10(a), and the amplitude values for all the visibility pairs are in the range 0.996 ± 0.017 to 1.001 ± 0.006. The CP values are shown in Fig. 10(b). For a small subset (i.e., <10%) of samples, we obtained $\pm 2\pi$ phase jumps, which are likely due to numerical errors, and are, thus, removed in Fig. 10(b). We observe the CP values consistent with 0° for all the triplets. When testing SR = 0.5, we find, as expected,

an even lower dispersion for the retrieved amplitudes and CP values. These results suggest that the effect of amplitude and phase residual errors from the AO should be negligible in comparison to other noise sources. In the subsequent sections, we considered additional sources of noise and considered only one visibility amplitude and one CP for a clearer demonstration of the resulting effects. We selected the visibility V_{14} and the CP Φ_{234}, which have the lowest mean squared error in Fig. 10.

B. Photon Shot Noise

As the output intensity images provided by Rsoft are normalized, we multiplied the images by a constant factor to get the number of photons (N_p) per pixel. Thus, a random Poisson distribution with a mean of N_p photons per pixel is now applied to the output image of DBC containing the intensity of the complex electric fields to obtain the required photon shot noise.

By setting N_p to the values 10^2, 10^3 and 10^4, we obtain different histograms of the visibility amplitude for the pair V_{14} as shown in Fig. 11(a). It can be seen that the standard deviation of the visibility amplitude distribution increases for low N_p where the effects of photon noise become more significant. As a result, there is a spread in the visibility amplitude distribution as N_p decreases. The histogram plot for the CP triplet Φ_{234} in Fig. 11(b) also shows a gradual increase of the standard deviation for decreasing N_p. In addition to the photon noise, the detector noise is added to the DBC outputs, and the impact on the visibilities is studied in the next section.

C. Detector Noise

We now consider the simultaneous contribution of the photon noise and detector noise. For the latter, we include two main components: (1) readout noise; (2) dark current (I_d). To implement these noises in our intensity images obtained from Rsoft, we converted N_p in Section 8.B into the number of electrons N_e using the 90% quantum efficiency of the CRED2 when operated at −40° C [39]. After N_e is calculated, we added a Gaussian random distribution for the readout electrons with a standard deviation of $22e^-$ per pixel [38] and added a Poisson random distribution for dark current with a mean of 600 e^-/s per pixel [39]. Successively, N_e is converted to analog-to-digital units (ADU) by multiplying it with the gain of the camera, which is 0.49 ADU/e^- [39]. Since $I_d \propto t_e$, we considered our on-sky $t_e = 250$ ms giving an $I_d = 150e^-$ per pixel. The distribution of the retrieved visibility amplitude is shown in Fig. 12(a) for three scenarios of N_p.
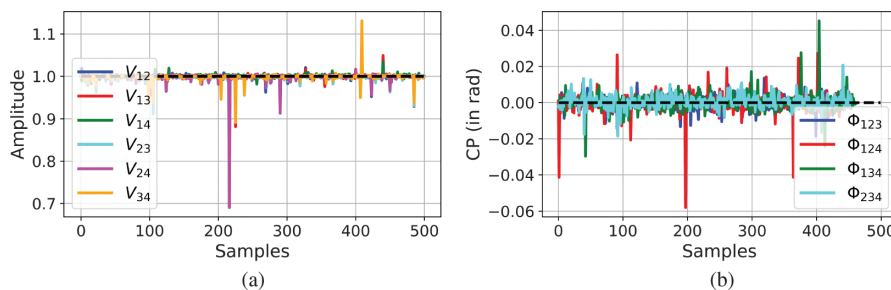

Fig. 10. Retrieved simulated visibilities with four input beams coupled into the DBC device. Both the amplitudes and phases vary following a statistical Gaussian distribution (see text for details). Black is the theoretical curve. (a) Visibility amplitudes. (b) Closure phases.
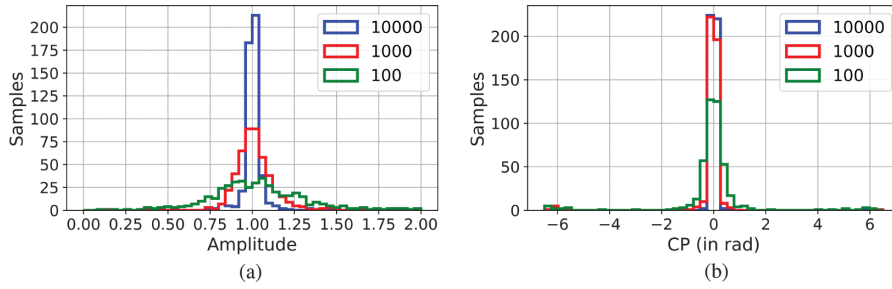
Fig. 11. Histogram of the retrieved visibilities for different levels of photon shot noise. The legend shows the mean number of photons N_p per pixel. (a) V_{14}. (b) Φ_{234}.
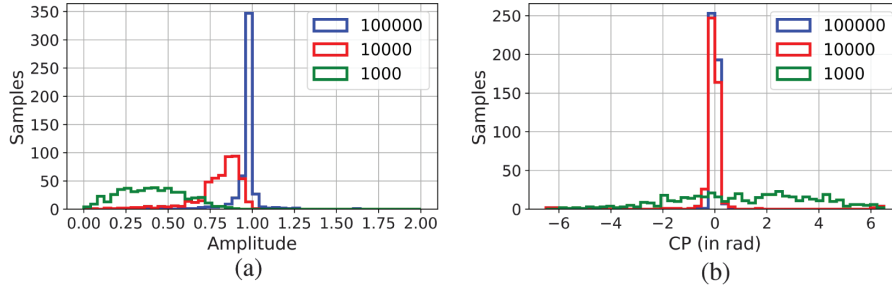

Fig. 12. Histogram of the retrieved visibilities for different levels of photon shot noise along with added detector noise (see Section 8.C for details). The legend shows the N_p per pixel. (a) V_{14}. (b) Φ_{234}.

In comparison to the photon noise dominated case (see Section 8.B), the inclusion of the detector noise produces a larger spread of the interferometric quantities with a decreasing number of photons N_p, but also clearly shifts the peak of the visibility amplitude distribution toward V < 1. The spread of the CP histograms is also significantly impacted when including the detector noise in the low photon regime. As we may have expected, this implies that in the low-flux regime, the detector noise in our experiment becomes dominant along with photon noise. This is a major source of signal degradation in the retrieval process of the coherence vector. In the next section, we discuss the effect of longer t_e on the retrieved visibility amplitude.

D. Effect of $t_e > \tau_0$

The use of AO acting as a fringe tracker allows in principle to increase the integration time t_e beyond the characteristic coherence time of the atmosphere τ_0. In the absence of AO correction, the standard deviation of the phase between the sub-apertures of our longest baseline 1–4 for the observing conditions reported in Table 3 is estimated to be ~1.6λ (Eq. 4.45, [40]), while it is only $\lambda/5$ with the AO correction. However, with a SR ~ 30%, it is possible that the level of residual phase error produces fringe smearing, which causes the retrieved visibility amplitudes to be smaller than unity.

To simulate the effect of longer t_e on a squared law detector, we take an intensity summation over n samples obtained in Section 8.A by fulfilling $n = t_e/\tau_0$. We also took into account the photon shot noise and detector noise, and tested for $n = 1$, 2, 4, 10. We show the median values of the retrieved visibility amplitudes for the pair V_{14} in Fig. 13(a) for SR = 0.3 and 0.5. The case $n = 1$ corresponds to $t_e \sim 30$ms with $N_p = 10^4$ photons per pixel. We observe the clear effect of fringe smearing
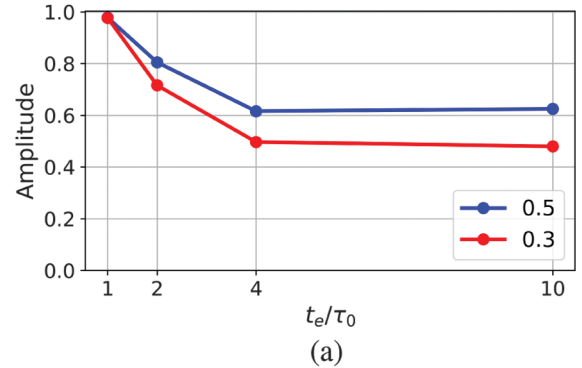

Fig. 13. Median value of the retrieved visibility amplitude (V_{14}) as a function of the exposure time. The legend shows the Strehl ratio. Here the case n = 1 assumes $t_e = 30$ ms with $N_p = 10^4$ photons per pixel.

due to partial AO correction, suggesting that the chosen value of the exposure time contributes to the drop in the visibility amplitude.

9. DISCUSSION AND CONCLUSION

We present in this paper the first on-sky testing of the integrated optics interferometric DBC concept, following numerous campaigns of laboratory testing. This is a major step since we had the opportunity to operate under real astronomical conditions. The DBC was designed to operate in the H-band and was integrated into a classical aperture masking/pupil remapping experiment at the 4.2 m WHT. Four sub-pupils forming a non-redundant array were coupled into our beam combiner taking advantage of the partial AO correction from the WHT. We observed the two bright single stars Vega and Altair [41] and retrieved the

complex coherence vectors making use of the calibrated transfer matrix of the system. Several points can be discussed.

• We were able to couple successfully stellar photons in the DBC and retrieve the visibility amplitudes for the two stars. For all the baselines, the visibility amplitude distributions were peaking below the expected value of $V = 1$ for an unresolved source, typically around $\sim 0.6-0.8$, with a significant dispersion around the mean value. The measured CPs also exhibit a significant dispersion around $0°$ and show in some cases departures from $0°$ that we do not interprete as an astrophysical signal. We conducted an extensive analysis work to interpret our observational results.

• Using our high-flux, turbulence-free, broadband calibration source, we observe that, in most cases, we were able to retrieve the visibility distributions in agreement with $V \sim 1$ and $CP \sim 0°$. However, we strongly believe that our calibrated transfer matrix (or V2PM) might be affected by biases, in part because we could not use the same camera for the V2PM calibration and the on-sky observation. This is detrimental to obtain precisely calibrated visibilities and CPs.

• The comparison between the high-flux case (i.e., with calibration source) and a case where no signal is detected at the DBC outputs clearly indicates that the shape, spread, and peak in the histograms of the retrieved quantities are strongly influenced by the reachable SNR at the 23 measured outputs. For Vega, we reached an SNR $\sim 2-10$, which we consider at the edge of measuring a coherent signal.

• We have run several simulations to understand the origin of the low visibilities and high dispersion. We find that: (1) The partial AO correction of $\sim 200-300$ nm rms is not by itself the main cause for the large dispersion of the data, but this level of correction and the relatively large exposure time compared to the atmosphere coherence time would result in fringe smearing, decreasing the value of the retrieved visibilities to ~ 0.5; (2) in the low photon regime of our DBC experiment, the impact of the detector noise is also very significant in shifting the distribution peaks and increasing the dispersion. This clearly affects the retrieved CPs, which in high-flux conditions would be otherwise more robust to the residual phase errors.

We have faced in this experiment some of the classical challenges of similar experiments [9,10]: With single apertures of ~ 50 cm in diameter and the need for short integration times, we quickly ended up in a low photon regime where the level of the AO correction, which does not permit exposure times significantly longer than τ_0, and the noise figure of the camera also played a major role.

For our on-sky DBC experiment, we briefly discuss our results in the context of similar experiments where medium-sized 2–4 m telescopes were employed. Huby *et al.* [9] operated in the visible range a pupil remapping experiment in which they were able to measure precise CPs, but could not measure visibility amplitudes. Jovanovic *et al.* [10] tested in the H-band a multi-axial combination scheme using a ULI written beam combiner. They show that they were able to detect fringes on a bright source and set constraints on the achievable precision on the CPs. In comparison, our retrieval of the CPs is not satisfactory to a level comparable to these authors, but it is not possible with this data to conclude if this is intrinsic to the DBC retrieval

process since we are strongly impacted by other sources of noise. On the other side, the retrieval of the visibility amplitude delivered a better outcome, even though we are impacted by fringe smearing.

In the future, an improved control of the stability of the experiment, and in particular of the waveguide injection, as well as a more rigorous determination of the V2PM transfer matrix, may reinforce the potential of DBC-based beam combination scheme.

REFERENCES

1. J. Baldwin, C. A. Haniff, C. Mackay, and P. Warner, "Closure phase in high-resolution optical imaging," Nature **320**, 595–597 (1986).
2. P. G. Tuthill, J. D. Monnier, W. C. Danchi, E. H. Wishnow, and C. A. Haniff, "Michelson interferometry with the Keck I Telescope," Publ. Astron. Soc. Pac. **112**, 555–565 (2000).
3. P. G. Tuthill, J. D. Monnier, and W. C. Danchi, "A dusty pinwheel nebula around the massive star WR104," Nature **398**, 487–489 (1999).
4. J. D. Monnier, P. G. Tuthill, M. Ireland, R. Cohen, A. Tannirkulam, and M. D. Perrin, "Mid-infrared size survey of young stellar objects: description of Keck segment-tilting experiment and basic results," Astrophys. J. **700**, 491–505 (2009).
5. N. Huélamo, S. Lacour, P. Tuthill, M. Ireland, A. Kraus, and G. Chauvin, "A companion candidate in the gap of the T Chamaeleontis transitional disk," Astron. Astrophys. **528**, L7 (2011).
6. A. L. Kraus and M. J. Ireland, "LkCa 15: a young exoplanet caught at formation?" Astrophys. J. **745**, 5 (2011).
7. B. Biller, S. Lacour, A. Juhász, M. Benisty, G. Chauvin, J. Olofsson, J.-U. Pott, A. Müller, A. Sicilia-Aguilar, M. Bonnefoy, P. Tuthill, P. Thebault, T. Henning, and A. Crida, "A likely close-in low-mass Stellar companion to the transitional disk star HD 142527," Astrophys. J. **753**, L38 (2012).
8. G. Perrin, S. Lacour, J. Woillez, and É. Thiébaut, "High dynamic range imaging by pupil single-mode filtering and remapping," Mon. Not. R. Astron. Soc. **373**, 747–751 (2006).
9. E. Huby, G. Perrin, F. Marchis, S. Lacour, T. Kotani, G. Duchêne, E. Choquet, E. L. Gates, J. M. Woillez, O. Lai, P. Fédou, C. Collin, F. Chapron, V. Arslanyan, and K. J. Burns, "First, a fibered aperture masking instrument—I. First on-sky test results," Astron. Astrophys. **541**, A55 (2012).
10. N. Jovanovic, P. G. Tuthill, B. Norris, S. Gross, P. Stewart, N. Charles, S. Lacour, M. Ams, J. S. Lawrence, A. Lehmann, C. Niel, J. G. Robertson, G. D. Marshall, M. Ireland, A. Fuerbach, and M. J. Withford, "Starlight demonstration of the Dragonfly instrument: an integrated photonic pupil-remapping interferometer for high-contrast imaging," Mon. Not. R. Astron. Soc. **427**, 806–815 (2012).
11. S. Minardi, S. Lacour, J.-P. Berger, L. Labadie, R. R. Thomson, C. Haniff, and M. Ireland, "Beam combination schemes and technologies for the Planet Formation Imager," Proc. SPIE **9907**, 99071N (2016).

12. GRAVITY Collaboration, R. Abuter and M. Accardo, and et al., "First light for gravity: phase referencing optical interferometry for the very large telescope interferometer," Astron. Astrophys. **602**, A94 (2017).

13. J.-B. Le Bouquin, J.-P. Berger, and B. Lazareff, and et al., "PIONIER: a 4-telescope visitor instrument at VLTI," Astron. Astrophys. **535**, A67 (2011).

14. R. G. Petrov, F. Malbet, and G. Weigelt, and et al., "AMBER, the near-infrared spectro-interferometric three-telescope VLTI instrument," Astron. Astrophys. **464**, 1–12 (2007).

15. N. Anugu, J.-B. L. Bouquin, J. D. Monnier, S. Kraus, B. R. Setterholm, A. Labdon, C. L. Davies, C. Lanthermann, T. Gardner, J. Ennis, K. J. C. Johnson, T. T. Brummelaar, G. Schaefer, and J. Sturmann, "MIRC-X: a highly sensitive six-telescope interferometric imager at the CHARA array," Astron. J. **160**, 158 (2020).

16. E. Tatulli, F. Millour, and A. Chelli, and et al., "Interferometric data reduction with AMBER/VLTI. Principle, estimators, and illustration," Astron. Astrophys. **464**, 29–42 (2007).

17. S. Minardi and T. Pertsch, "Interferometric beam combination with discrete optics," Opt. Lett. **35**, 3009–3011 (2010).

18. M. Benisty, J. P. Berger, L. Jocou, P. Labeye, F. Malbet, K. Perraut, and P. Kern, "An integrated optics beam combiner for the second generation VLTI instruments," Astron. Astrophys. **498**, 601–613 (2009).

19. E. Pedretti, J. D. Monnier, T. ten Brummelaar, and N. D. Thureau, "Imaging with the CHARA interferometer," New Astron. Rev. **53**, 353–362 (2009).

20. E. Pedretti, S. Piacentini, G. Corrielli, R. Osellame, and S. Minardi, "A six-apertures discrete beam combiners for J-band interferometry," Proc. SPIE **10701**, 316–325 (2018).

21. A. Saviauk, S. Minardi, F. Dreisow, S. Nolte, and T. Pertsch, "3D-integrated optics component for astronomical spectro-interferometry," Appl. Opt. **52**, 4556–4565 (2013).

22. R. Diener, J. Tepper, L. Labadie, T. Pertsch, S. Nolte, and S. Minardi, "Towards 3D-photonic, multi-telescope beam combiners for mid-infrared astrointerferometry," Opt. Express **25**, 19262–19274 (2017).

23. A. S. Nayak, T. Poletti, T. K. Sharma, K. Madhav, E. Pedretti, L. Labadie, and M. M. Roth, "Chromatic response of a four-telescope integrated-optics discrete beam combiner at the astronomical l band," Opt. Express **28**, 34346–34361 (2020).

24. I. C. Ipsen, *Numerical Matrix Analysis: Linear Systems and Least Squares* (SIAM, 2009).

25. S. Minardi, "Nonlocality of coupling and the retrieval of field correlations with arrays of waveguides," Phys. Rev. A **92**, 013804 (2015).

26. P. Tuthill, J. Lloyd, M. Ireland, F. Martinache, J. Monnier, H. Woodruff, T. ten Brummelaar, N. Turner, and C. Townes, "Sparse-aperture adaptive optics," Proc. SPIE **6272**, 1064–1073 (2006).

27. R. C. Jennison, "A phase sensitive interferometer technique for the measurement of the Fourier transforms of spatial brightness distributions of small angular extent," Mon. Not. R. Astron. Soc. **118**, 276–284 (1958).

28. P. Lawson, *Principles of Long Baseline Stellar Interferometry* (JPL, 2000).

29. N. Charles, N. Jovanovic, S. Gross, P. Stewart, B. Norris, J. O'Byrne, J. S. Lawrence, M. J. Withford, and P. G. Tuthill, "Design of optically path-length-matched, three-dimensional photonic circuits comprising uniquely routed waveguides," Appl. Opt. **51**, 6489–6497 (2012).

30. A. Arriola, S. Gross, N. Jovanovic, N. Charles, P. G. Tuthill, S. M. Olaizola, A. Fuerbach, and M. J. Withford, "Low bend loss waveguides enable compact, efficient 3D photonic chips," Opt. Express **21**, 2978–2986 (2013).

31. G. Corrielli, S. Atzeni, S. Piacentini, I. Pitsios, A. Crespi, and R. Osellame, "Symmetric polarization-insensitive directional couplers fabricated by femtosecond laser writing," Opt. Express **26**, 15101–15109 (2018).

32. R. J. Harris, T. K. Sharma, J. J. Davenport, P. Hottinger, T. Anagnos, A. S. Nayak, A. Quirrenbach, L. Labadie, K. V. Madhav, and M. M. Roth, "NAIR: novel astronomical instrumentation through photonic reformatting," Proc. SPIE **11451**, 18–31 (2020).

33. A. S. Nayak, T. K. Sharma, L. Labadie, S. Piacentini, G. Corrielli, R. Osellame, É. Gendron, J.-T. M. Buey, F. Chemla, M. Cohen, N. A. Bharmal, L. F. Bardou, L. Staykov, J. Osborn, T. J. Morris, E. Pedretti, A. N. Dinkelaker, K. V. Madhav, and M. M. Roth, "First on-sky results with an interferometric discrete beam combiner (DBC) at the William Herschel Telescope," Proc. SPIE **11446**, 360–372 (2020).

34. B. R. Norris, N. Cvetojevic, T. Lagadec, N. Jovanovic, S. Gross, A. Arriola, T. Gretzinger, M.-A. Martinod, O. Guyon, J. Lozi, M. J. Withford, J. S. Lawrence, and P. Tuthill, "First on-sky demonstration of an integrated-photonic nulling interferometer: the glint instrument," Mon. Not. R. Astron. Soc. **491**, 4180–4193 (2020).

35. R. M. Myers, Z. Hubert, T. J. Morris, E. Gendron, N. A. Dipper, A. Kellerer, S. J. Goodsell, G. Rousset, E. Younger, M. Marteaud, A. G. Basden, F. Chemla, C. D. Guzman, T. Fusco, D. Geng, B. L. Roux, M. A. Harrison, A. J. Longmore, L. K. Young, F. Vidal, and A. H. Greenaway, "CANARY: the on-sky NGS/LGS MOAO demonstrator for EAGLE," Proc. SPIE **7015**, 52–60 (2008).

36. E. Gendron, F. Vidal, and M. Brangier, and et al., "MOAO first on-sky demonstration with canary," Astron. Astrophys. **529**, L2 (2011).

37. E. Gendron, T. Morris, and A. Basden, and et al., "Final two-stage MOAO on-sky demonstration with CANARY," Proc. SPIE **9909**, 126–142 (2016).

38. R. K. Gibson, R. Oppenheimer, C. T. Matthews, and G. Vasisht, "Characterization of the C-RED 2: a high-frame rate near-infrared camera," J. Astron. Telesc. Instrum. Syst. **6**, 011002 (2019).

39. "C-RED 2 data sheet," https://www.first-light-imaging.com/wp-content/uploads/2019/02/Datasheet_C-RED-2_17.11.2020.pdf.

40. A. Glindemann, *Principles of Stellar Interferometry* (Springer, 2011).

41. G. T. van Belle, D. R. Ciardi, R. R. Thompson, R. L. Akeson, and E. A. Lada, "Altair's oblateness and rotation velocity from long-baseline interferometry," Astrophys. J. **559**, 1155–1164 (2001).